

Adaptive Neutron Radiography Correlation for Simultaneous Imaging of Moisture Transport and Deformation in Hygroscopic Materials

S.J. Sanabria · C. Lanvermann · F. Michel · D. Mannes · P. Niemz

Received: 13 March 2014 / Accepted: 18 September 2014 / Published online: 21 October 2014
© Society for Experimental Mechanics 2014

Abstract Neutron radiography is a key non-destructive testing technology for the investigation of moisture transport in materials. However, quantitative moisture measurements in swelling materials are currently challenging due to the lack of referencing between moist and dry state radiographs. A novel adaptive texture correlation algorithm is presented to simultaneously image inhomogeneous moisture distributions and moisture-induced strain fields. The proposed method provides a valuable tool for the study of time- and position-dependent hygromechanical interactions. Moreover, it requires no modification of existing neutron installations. The method was validated against gravimetric moisture content and optic surface deformation measurements. Its applicability was demonstrated for two actual topics in wood science, the investigation of moisture gradients within the growth ring microstructure and the study of moisture transport processes in wood-fiber composites. The algorithm can be widely used to characterize hygroscopic materials with heterogeneous

texture, as frequently found in wood constructions, food industry, engineering and soil science.

Keywords Non-destructive neutron imaging · Heterogeneous texture correlation · Moisture-induced deformation strains · Wood composite materials · Mechano-sorptive rheology

Introduction

Neutron imaging (NI) is an established method to non-destructively study the dynamics of hydrogenous fluids, such as bound (hygroscopic) or free water molecules, in geomaterials (rocks, soils), engineered media (ceramics, polymers, metals, concrete, fuel cells, heat pipes, engines...) and biological composites (wood, food, natural fiber-reinforced composites...), among others. Compared to X-ray and Nuclear Magnetic Resonance (NMR) imaging, NI is highly sensitivity to hydrogen while being transparent to most solid-state materials, including heavy metals. Moreover, it allows dynamic full-field imaging in two (radiography) and three (tomography) dimensions with tenth-of-millimeter spatial resolution and sub-second measurement times [1–5].

Moisture intake in porous media is often accompanied by swelling, which is especially relevant for biological composites [6]. Wood is a classical example, volumetric swelling strains >10 % are not rare within its large hygroscopic range, which goes up to 30 % moisture content from oven-dry state until the fiber saturation point (FSP), due to the hydrophilic behavior of the lignocellulosic cell walls. If not accounted for, swelling strain gradients can impair dimensional stability and induce eigenstresses, leading to cracking and delamination, which reduce the serviceability of wooden constructions [7]. Natural fiber-reinforced composites have drawn widespread attention in the last decades due to their low cost and biodegradability, accompanied by high strength and insulation

Electronic supplementary material The online version of this article (doi:10.1007/s11340-014-9955-2) contains supplementary material, which is available to authorized users.

S.J. Sanabria (✉) · C. Lanvermann · F. Michel · P. Niemz
Institute for Building Materials ETH Zurich, Stefano-Francini-Platz
6, CH-8093 Zurich, Switzerland
e-mail: ssanabria@ethz.ch

C. Lanvermann
e-mail: lanvermannchr@ethz.ch

F. Michel
e-mail: frmichel@ethz.ch

P. Niemz
e-mail: niemzp@ethz.ch

D. Mannes
Neutron Imaging and Activation Group, Paul Scherrer Institute,
CH-5232 PSI, Villigen, Switzerland
e-mail: david.mannes@psi.ch



properties [8]. However, their highly hygro-morphic behavior is challenging. For example, the inner stresses induced in the hot pressing of wood-based fiber composites lead to larger thickness swelling than in raw wood material [9]. The coupling between moisture transport and deformation is also a key element to describe food drying, clay consolidation and sorption in polymer electrolyte fuel cells. Although sophisticated hygro-mechanical models are available, they often lack of accompanying experimental data. In this context, the simultaneous full-field imaging of moisture and moisture-induced deformation is necessary [6, 10–14].

Quantitative moisture measurements with neutrons also require hygro-expansion data. The gravimetric moisture content $\omega = m_h/m_o$ is defined in terms of the mass m_h of water with respect to the mass of the dry solid phase m_o , which requires the local referencing of the neutron radiographs in moist T state to the dry state T_o . Moreover, the density of the solid phase is lower in moist than in dry state due to sample swelling. Thus the in-plane swelling strain fields ε_{ii} with respect to the reference dry state (Lagrangian description) need to be included in the calculation of ω (Equation 1) [11, 15]:

$$\omega = (1 + \varepsilon_{XX})(1 + \varepsilon_{YY})\rho_h z_h (\rho_o l_z)^{-1} \quad (1)$$

with l_z the sample thickness, ρ_h and ρ_o the densities of water (10^3 kg m^{-3}) and dry solid phase substance, respectively, and z_h the effective water column thickness (Equation 2):

$$Z_h = -[(\Sigma/\rho)_h \rho_h]^{-1} [\ln T - \ln T_o (1 + \varepsilon_{XX})^{-1} (1 + \varepsilon_{YY})^{-1}] \quad (2)$$

$$\rho_o = -\ln T_o [(\Sigma/\rho)_o l_z]^{-1}$$

$(\Sigma/\rho)_h$ and $(\Sigma/\rho)_o$ are respectively the mass-attenuation coefficients in water and solid phases. For the energy spectrum of the thermal neutron beamline NEUTRA at the Paul Scherrer Institute (Villigen, Switzerland) [41], where the presented investigations were carried out, $(\Sigma/\rho)_o = 0.18 \text{ m}^{-2} \text{ kg}^{-1}$ for wood (Table 1, [42]) and $(\Sigma/\rho)_h = 0.35 \text{ m}^{-2} \text{ kg}^{-1}$ for water [43]. Operating Equation 1 shows that neglecting hygroscopic strains of 10 % in wood leads to unacceptable quantitative moisture errors over 5 % (absolute error), as shown in Equation 3:

$$\omega = \omega|_{\varepsilon=0} [1 + \varepsilon_{XX} + \varepsilon_{YY}]$$

$$+ (\Sigma/\rho)_o [(\Sigma/\rho)_h]^{-1} [\varepsilon_{XX} + \varepsilon_{YY} + \varepsilon_{XX}\varepsilon_{YY}] \approx \omega|_{\varepsilon=0}$$

$$+ 0.52[\varepsilon_{XX} + \varepsilon_{YY}] \quad (3)$$

Finally, the edge misalignment induced by hygro-expansion leads to unbounded errors and non-physical moisture values at image discontinuities, which impedes or makes

the study of moisture transport through multi-layered composites and surface coatings challenging [16, 17].

These shortcomings have so far been alleviated with a global pre-registering of neutron radiographs based on sample edge detection [18–21], which reduces edge misalignment, but does not account for inner deformation gradients. Full-field strain measurements with neutrons have been achieved in some crystalline materials by using a tunable monochromatic beam, for which Bragg cut-off wavelengths provide lattice spacing [1]. Yet a combination with moisture measurements has not been reported. NI was recently combined with optical deformation measurements [15]. Although accurate high-resolution ε_{ii} measurements were obtained, the setup requires sample speckling and an involved synchronized camera installation. Moreover, only surface deformation is measured, which leads to significant edge misalignment artifacts in volumetric samples.

In this work, a novel Adaptive Neutron Radiography Correlation (ANRC) algorithm is presented, which uses the texture information in neutron images to locally estimate the strain fields. This method is exclusively based on the postprocessing of radiographs, therefore requiring no modification of existing neutron installations, and providing average deformation estimates over the sample thickness. The new approach is validated with gravimetric and optic methods. Its potential and applicability are demonstrated for two actual research topics in wood science:

- a) Gradients in moisture and hygroscopic swelling in soft-wood growth rings [15, 16, 22–25]
- b) Investigation of moisture transport through swelling wood-fiber composites [3, 17, 18, 26]

Adaptive Neutron Radiography Correlation (ANRC)

The starting point for the ANRC algorithm is a set of neutron radiographies of the test samples, which are experimentally acquired at well-controlled dry and moist states. State of the art corrections are first applied to compensate for source and detector inhomogeneities (CCD dark current, median filter, intensity normalization, flat field correction, spectral effects), background scattering (black body calibration) and sample scattering (Monte-Carlo simulations) [43].

Figure 1 summarizes the building blocks of the ANRC algorithm. The inner core performs *Digital Image Correlation* (DIC) processing. Subsets of the reference image I^{ef} (dry state) are automatically searched at specific positions r of the deformed image I^{est} (moist state), resulting in local estimates of the deformation vector $u(r)$, from which the strains fields ε_{ij} are differentiated. The DIC method is well-known and performs best for artificial random speckle

Table 1 Summary of neutron attenuation properties, ANRC settings and correlation statistics for the investigated test materials

	ρ_o (kg m ⁻³)	$(\Sigma/\rho)_o$ (m ² kg)	d (m)	Δ (mm) ^b	s_{ρ}/ρ (%) ^c	CNR (a.u.) ^c	r (a.u.)	$e=1$ (%)	u^{\max} (mm)
I: Optical, softwood growth rings ^a (Fig. 2, 4.1.1)	n.a. (not applicable)	n.a.	n.a.	[0.2, 0.2]	n.a.	4.6	0.96	[0.7, 0.7]	[1.5, 1.0]
II: Neutron, softwood growth rings ^a (Fig. 3–6, 4.1.2)	362	0.18	0.005	[2.9, 2.9]	34	5.1	0.98	[0.5, 16]	[0.8, 1.7]
III: Neutron, wood-fiber composites ^a (Fig. 7–8, 4.2)									
Isonat chanvre	44	0.27	0.04	[4.5, 9]	15	2.5	0.92	[0, 0]	[0.2, 0.04]
Pavaflex	48	0.23	0.04	[4.5, 9]	16	2.5	0.91	[0, 0]	[0.2, 0.08]
Pavatherm	135	0.19	0.04	[4.5, 9]	6	1.2	0.76	[0, 0]	[0.1, 0.04]
Aerogel Vliesmatte	147	0.10	0.04	[4.5, 9]	9	1.6	0.88	[0, 0]	[0.3, 0.2]
Isoroof-natur-KN	225	0.18	0.04	[4.5, 9]	6	1.1	0.64	[1.6, 1.4]	[0.6, 0.2]

^a The pixel sizes for I, II and III are 23, 77 and 145 μm, respectively

^b Fixed algorithm settings (px): $W_S=[3, 3]$, $W_L=[5, 5]$, $\Delta u^{\max}=[3, 3]$, $N_e=5$, $N_{\hat{u}}=[10, 100]$

^c s_{ρ} is the standard deviation of the dry material density ρ_o within the correlated subsets. $CNR=s_{\Delta}/s_n$, with s_{Δ} and s_n respectively for correlation subset and background image noise. $s_{\Delta}=s_{\rho}(\Sigma/\rho)_o I_Z \exp[-\rho_o(\Sigma/\rho)_o I_Z]$ for the neutron images T , following from Equation 2. $s_n=0.02$ for all radiographs

patterns, where unique subset correspondence is satisfied. Typical DIC parameters are subset size, search function and region and deformation order [27]. Many heterogeneous materials show enough natural texture to track u without need of artificial sample speckling, the DIC process is then specifically termed *Texture Correlation* (TC) [28]. Neutron radiographs of wood composites are assumed to show enough texture for TC, which is empirically confirmed by the high correlation statistics observed in the investigated test samples (Table 1).

The proposed ANRC processing is thus a TC algorithm, which is optimized and expanded to robustly extract deformation information from NI radiographs while ignoring “shadow regions”, where only poor correlation statistics are available. With this purpose, the DIC core implements a zero-order search (rigid subsets). A zero-normalized cross-correlation function I^{corr} (Equation 4) is calculated at each integer pixel position within a search window W for a subset size Δ . The peak maximum r provides the displacement vector u , which is refined by applying bicubic interpolation to I^{corr} :

$$I_{corr}(\hat{x}, \hat{y}) = \left(\frac{\sum_{x,y \in \Delta} [T(x-\hat{x}, y-\hat{y}) - \bar{T}] [T_o(x, y) - \bar{T}_o]}{\sum_{x,y \in \Delta} [T(x-\hat{x}, y-\hat{y}) - \bar{T}]^2 \sum_{x,y \in \Delta} [T_o(x, y) - \bar{T}_o]^2} \right)^{-1} \quad \mathbf{u} = \arg \max_{\hat{x}, \hat{y} \in \mathbf{W}} I_{corr} \quad (4)$$

In order to minimize false correlation hits, the search region is adaptively adjusted. The algorithm starts searching in a large reset window W_R . Subsequent search positions \hat{r}^i are ordered in a raster scan of the reference image. For each of them, the search is reduced to a shorter window W_S centered at an initial deformation estimate \hat{u} , which is calculated based on the linear extrapolation of $N_{\hat{u}}$ neighboring pixels. An error control block ensures the well-posing of the estimated u by controlling its: a) *correlation*: the correlation coefficient r is above a minimum threshold r^{\min} , b) *uniqueness*: u is within image bounds, is not an edge pixel of I^{corr} , and does not exceed a maximum deformation value u^{\max} , c) *continuity*: u does not increase by more than Δu^{\max} in each iteration. In the case of an error of type b), a

second trial is admitted with a larger window W_L before discarding u . Only non-error u values ($e=0$) are used for the adaptive search and the continuity error check. Ill-posed u ($e \neq 0$) increment the error count c_e up to a threshold N_e . Then the reset control block starts operation, deactivating the adaptive search and resetting the search window to W_R . The algorithm manages errors along individual dimensions of the deformation vector u_j by only storing well-posed u_j . The loss of continuity upon reset is additionally avoided by managing an additional reset count c_R and not accepting u values at first reset positions ($c_R=1$) for updating the deformation estimate \hat{u} , by using at reset positions \hat{u} instead of u for continuity control, and by filtering out isolated u pixels.

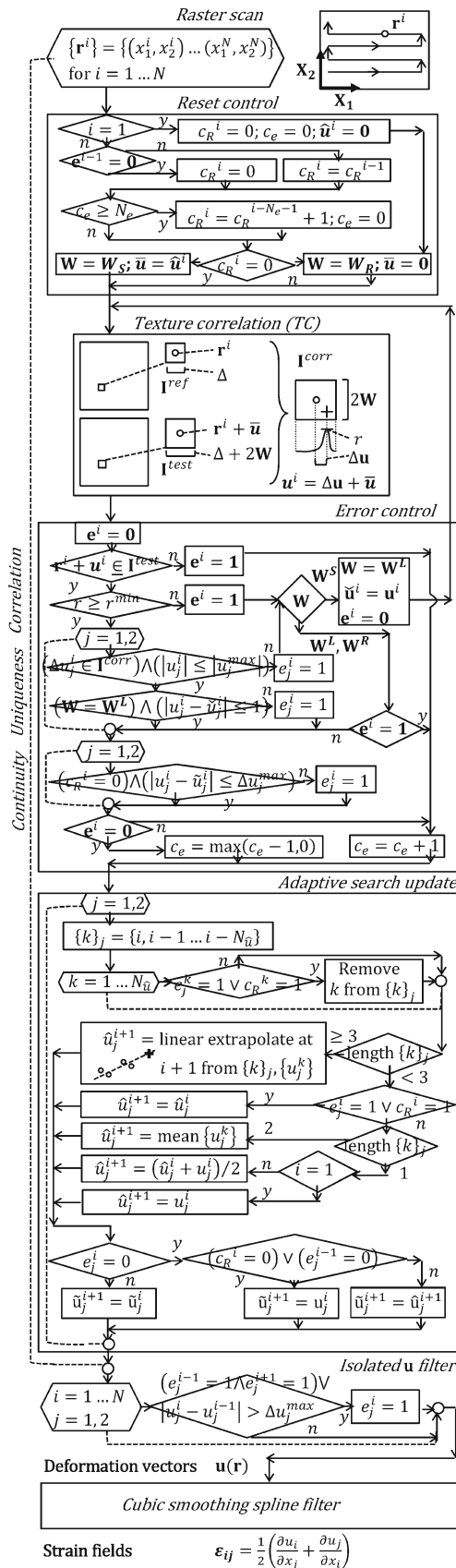


Fig. 1 Flow diagram of ANRC algorithm

Continuous deformation fields are calculated by fitting the estimated deformation vectors u to *cubic smoothing splines* $f(r^i)$ (Equation 5), which trade-off between data fidelity and smoothness [29]:

$$\sum_{i=1}^N r^i |u_j^i - f(r^i)|^2 + (1-p) \int D^2 |f(t)|^2 dt \quad p = (1 + h^3/6)^{-1} \quad (5)$$

The weights of the error function are adjusted to the peak correlation coefficients r . The resolution h , which controls the smoothness, is adjusted with the subset size in the range $h = \Delta/3 \dots \Delta$. The fitted spline functions are finally differentiated to compute the strain fields ϵ_{ij} . In order to minimize noise sensitivity, only first order derivatives are included in $\epsilon_{ij} = 0.5(\partial u_i / \partial x_j + \partial u_j / \partial x_i)$.

The settings of ANRC for each case study are summarized in Table 1. The subset size Δ is a trade-off between well-posing and lateral resolution of u . A threshold Δ is typically found, above which correlation statistics do not significantly improve. The ANRC algorithm was implemented in Matlab® (R2011b, The Mathworks Inc., Natick, MA, USA) and is provided in the supplementary materials for free use and development (Supp. Mat.).

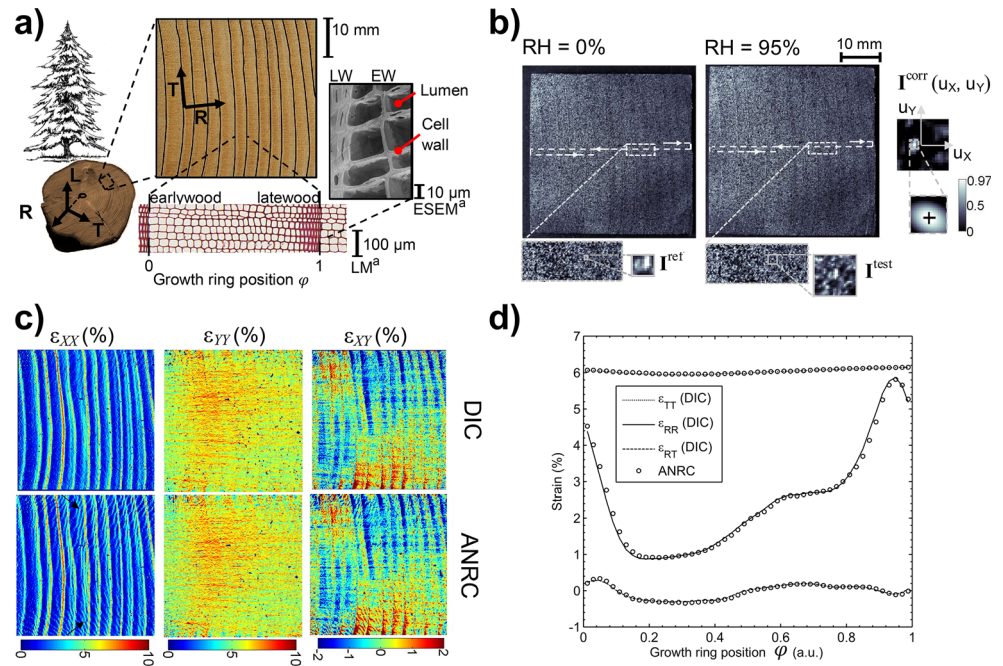
Experiments

Moisture and Swelling Gradients in Softwood Growth Rings at Hygroscopic Equilibrium

Optical surface deformation measurements

The strain field ϵ_{ij} calculation with ANRC was first quantitatively validated against a commercial DIC tool (VIC 2D 2009, Correlation Solutions Inc., USA) for high-resolution optical images of speckled softwood (Fig. 2). The DIC measurements were previously used to investigate wood cross-grain hygro-expansion at the growth ring structural level [15, 24]. The goal was to identify swelling strain gradients between the alternating bands of low-density earlywood (EW)– thin-wall wood cells with large internal lumens grown in spring – and high-density latewood (LW) – thick-wall cells with small-sized lumens grown in summer (Fig. 2a). Four cuboid samples ($40 \times 40 \times 5 \text{ mm}^3$) were cut from a Norway spruce (*Picea abies* Karst.) stem, their edges were well-aligned with respect to the main wood material axes (radial R \times tangential T \times longitudinal L). The samples were sprayed with a black/white speckle pattern by means of an airbrush gun with a nozzle size of 0.2 mm. They were then subjected in a portable climatic chamber to a moisture sorption–desorption cycle with relative humidity (RH) adjusted in 15 % steps between 0 and 95 %. For each nominal RH state, the samples were conditioned to equilibrium moisture content and optical images were acquired with a CCD camera (Fig. 2b). The

Fig. 2 Quantitative validation of ANRC processing on high-resolution CCD camera images. a) Test Norway spruce samples. The growth ring microstructure is illustrated at cellular scale with LM and at subcellular scale with ESEM. b) Optical surface images at dry (RH=0 %) and moist (RH=95 %) states, correlation subsets I^{ref} , I^{test} and search functions I^{corr} are highlighted. c) shows hygroscopic strain fields calculated from b) with both ANRC and a commercial DIC tool, which in d) are averaged and plotted in function of the growth ring position φ



^aLM: Light microscopy, ESEM: Environmental scanning electron microscopy

oven-dry state (RH=0 %) was used as reference. Next, the in-plane swelling strains were calculated with ANRC and compared to the commercial DIC results (Fig. 2c). The subset size Δ was 9×9 pixels² for both methods, for a pixel size of 23 μ m. Finally, the strains were transformed with respect to the material axes (R, T) and plotted in function of the relative growth ring position $\varphi=0 \dots 1$, with 0 and 1 respectively defining EW and LW regions (Fig. 2d). The coordinate transformation method is further detailed in [15, 24].

Simultaneous neutron imaging of moisture content and moisture-induced deformation

The moisture and strain gradients within the growth rings were investigated at equilibrium conditions with NI at the thermal neutron beam line NEUTRA at the Paul Scherrer Institute in Villigen, Switzerland. The experimental setup consists of a neutron beam collimator, a neutron detector and a portable climate chamber (Fig. 3a) and has been detailed in [15]. The neutron radiographs (Fig. 3b) show a pixel size of 145 μ m and a lateral resolution of ~ 0.7 mm (minimum detectable line spacing). The deformation vectors u and strain fields ε_{ij} at each RH step were computed with ANRC and a subset size Δ of 21×21 pixels² (Fig. 4). The moisture content distribution ω was calculated with Equation 1 and plotted in function of the growth ring position (Fig. 5).

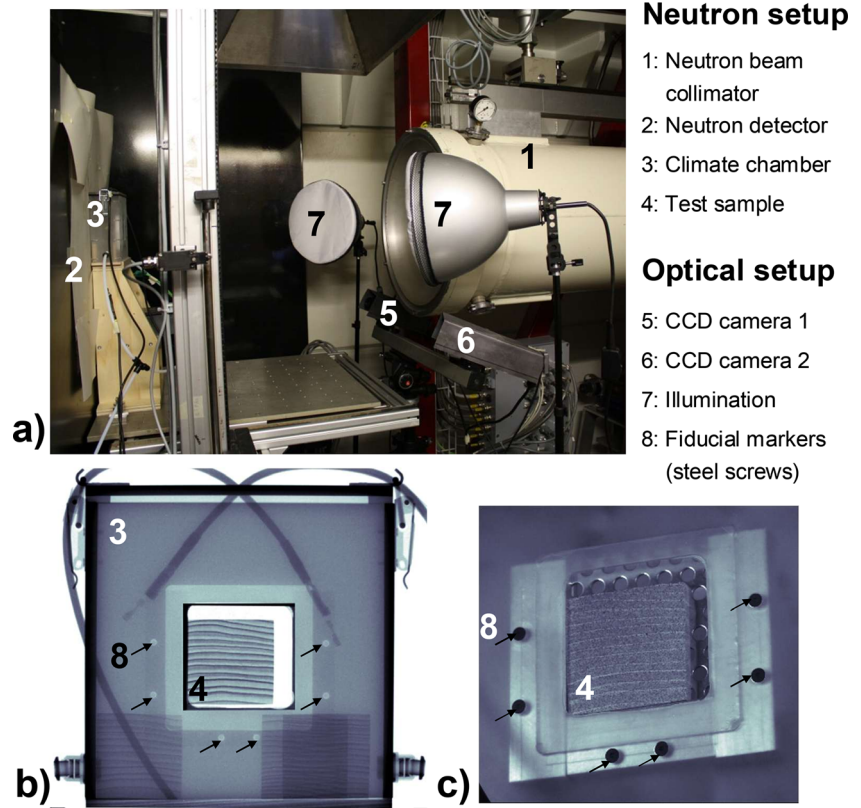
The average ω values were validated gravimetrically (Fig. 6). At each RH state the weight of the sample was recorded with 0.1 mg accuracy with a precision scale. The local moisture and strain fields were validated with the combined NI and optical

surface deformation measurement setup of [15]. With this purpose, a stereo-vision installation (Fig. 3a) consisting of two radiation-shielded CCD cameras and cold-light illumination captured optical images from the sample laterals without perturbing the neutron line of sight. The surface deformation vectors u were then calculated with commercial DIC (VIC3D, Correlated Solutions). As in 3.1.1, a subset size Δ of 9×9 pixels² was used, the resolution was here lower due to the optical constraints (pixel size 77 μ m). The optical images (Fig. 3c) and the neutron radiographs were referenced with fiducial markers. The calculated deformation vectors were then used to align the neutron radiographs and to compute ω .

Transient moisture diffusion and moisture-induced swelling in wood-fiber composites

The applicability of the ANRC algorithm to simultaneously investigate dynamic moisture transport and the large coupled deformations in biological composites was demonstrated for a selection of multi-layer building insulation materials. Three commercial wood fiberboards (Pavaflex, Pavatherm and Isoroof-natur-KN from Pavatex SA, Fribourg, Switzerland), a hemp fiber composite (Isonat chanvre from Valnaturel SA, Saxon, Switzerland) and a nanoporous aerogel (Aerogel Vliesmatte from Aspen Aerogels Inc., Northborough, MA, USA) were tested (Table 1). The material properties are detailed in [26, 30]. The test objects (40×40 mm² section) were typical three-layer insulation combinations, with two 20 mm thick Isoroof outer layers and a 35 mm (Isonat, Pavatherm, Pavaflex) or a 5 mm thick (Aerogel) middle layer. Following

Fig. 3 a) Neutron transmission setup for imaging of moisture-induced deformation, together with optical feedback for validation of ANRC strain field estimation. Sample neutron radiographs b) and CCD camera images c) are also shown



the experimental setup of [3, 17], six samples were oven-dried, sealed with aluminum tape on the four lateral surfaces and placed in a climatic box (RH=84 %, T=31 °C) above a desiccating silica gel. This ensures a unidirectional moisture transport from top to bottom sample surfaces. Neutron

radiographs were regularly acquired at NEUTRA during 17 h (same 145 μm pixel size as in 3.1.2) (Fig. 7a). To highlight the natural texture in the images, for each vertical position, the mean value was subtracted from the horizontal profiles, which were subsequently normalized to their

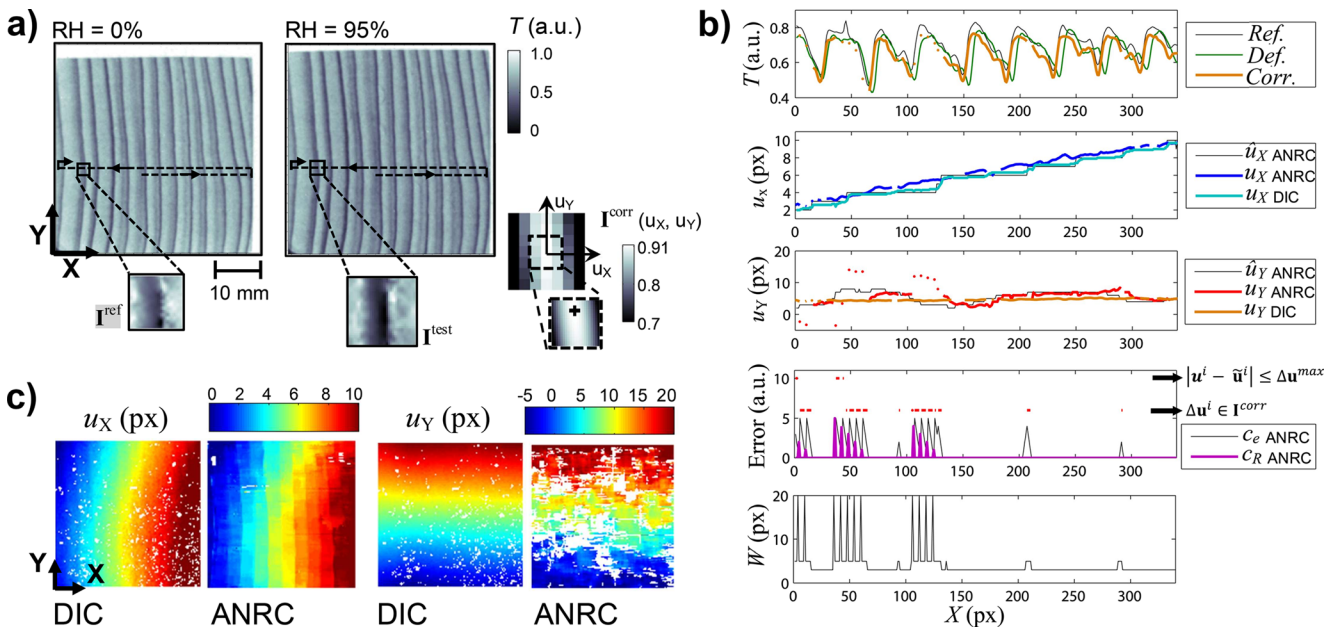
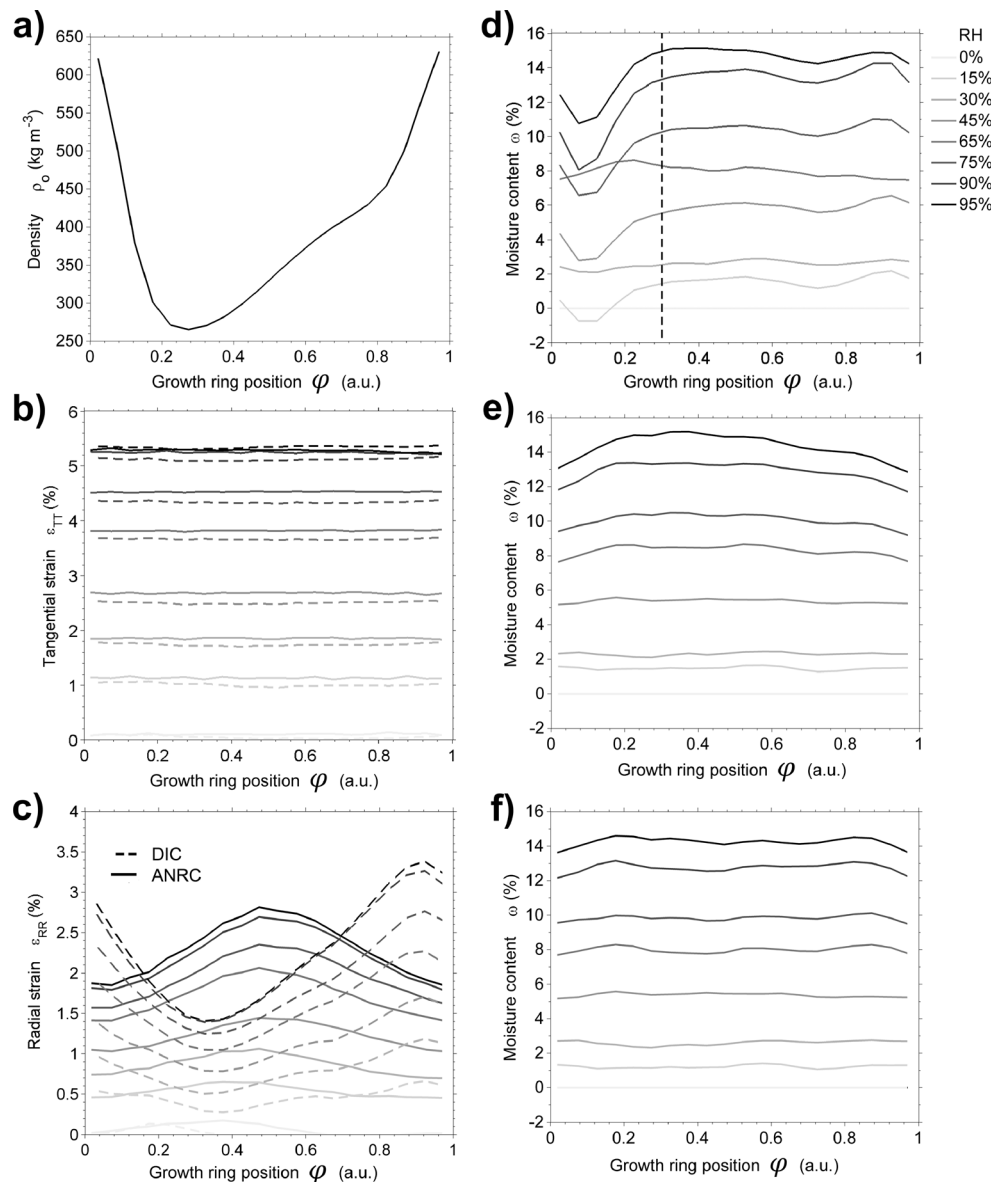


Fig. 4 Quantitative validation of ANRC processing on neutron images. a) Neutron radiographs corresponding to the test Norway spruce sample of Fig. 2. b) Evolution of ANRC variables during

raster scan of layered growth ring structure. c) Comparison of deformation fields calculated directly from neutron radiographs (ANRC) with respect to optic surface measurements (DIC)

Fig. 5 Moisture and swelling gradients within Norway spruce growth rings at hygroscopic equilibrium. a) Average density profile ρ estimated from neutron measurements. b) and c) show the strain fields ε_{TT} and ε_{RR} measured with the optical setup of Fig. 4a (DIC) and directly estimated from the neutron radiographs (ANRC). Moisture content profiles were calculated: by using DIC d) and ANRC e) for both neutron radiograph registration and swelling strain estimation, and f) by using ANRC for radiograph registration and DIC for swelling strain estimation



standard deviation (Fig. 7b). The images were then processed with ANRC with a subset Δ of 31×61 pixels² (thickness $Y \times$ width X) to calculate strain fields (Fig. 7c) and moisture concentrations (Fig. 7d).

Under fiber saturation, moisture transport in wood occurs due to diffusion, both as water vapor in the cell lumens and as bound water in the cell walls. The mass portion of water vapor is very small, leading to negligible neutron attenuation, the bound water concentration scales with ω . The unsteady-state diffusion is in a first approximation described by Fick’s second law [17]:

$$\partial_t \omega = \partial_y (D_{US} \delta_y \omega) \tag{6}$$

The diffusion coefficients D_{US} ($\text{m}^2 \text{s}^{-1}$) for each material layer were iteratively optimized [17, 18] by fitting the

experimental time-dependent moisture fields $\omega(x,y,t)$ to finite-difference time-domain solutions of Equation 6 (Fig. 8a). The results were compared to average steady state coefficients D_{SS} calculated with the standardized dry/wet cup method for each of the materials [26] (Fig. 8b). Finally, the time-evolution of the hygroscopic strains with respect to ω was investigated (Fig. 8c-e).

Results and Discussion

The comparison of ANRC correlation statistics for specific test scenarios shows distinctive trends (Table 1). The texture quality is well-summarized with a contrast to noise ratio CNR between the standard deviation of the correlation subset s_{Δ}

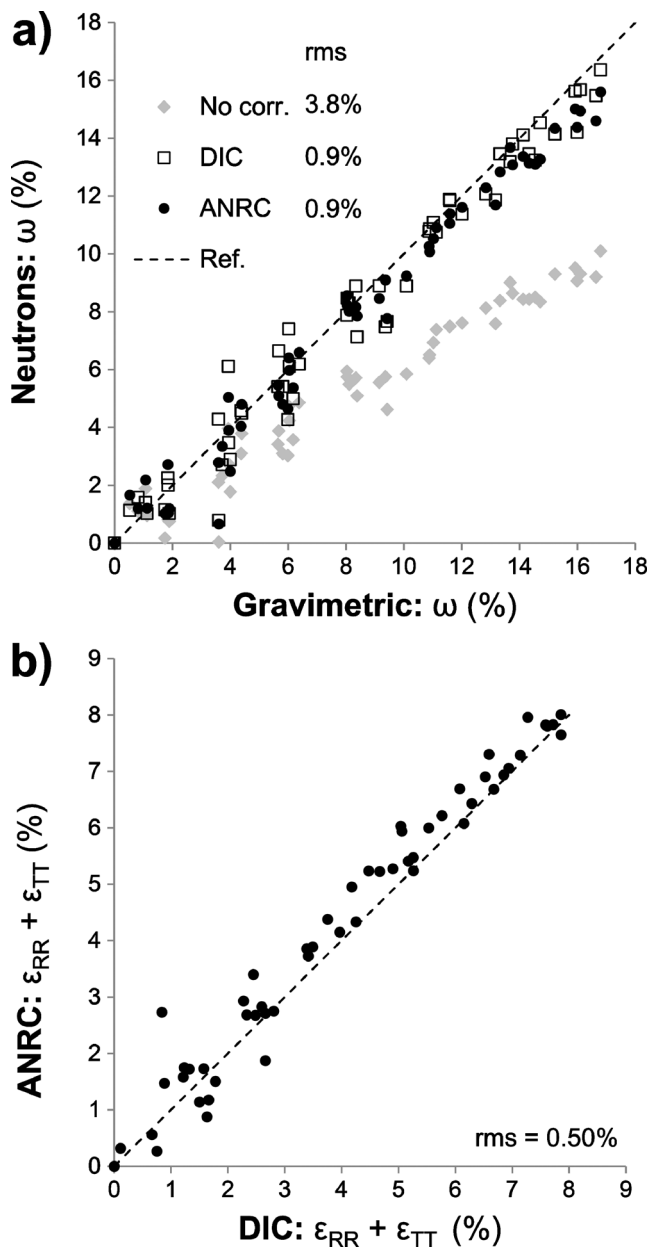


Fig. 6 a) Comparison of average gravimetric moisture content ω for each test sample with neutron values obtained without correction for hygroscopic swelling (no corr.), by using the optical setup of Fig. 4a for the correction (DIC), and by estimating the swelling fields directly from the radiographs (ANRC). b) Comparison of average swelling strains calculated with ANRC and DIC

and the background image noise s_n . Higher CNR lead to larger correlation coefficients r and, for the same image resolution, allow for smaller subset sizes Δ . The CNR is directly correlated with the density variability within the subset s_ρ/ρ . For wood-fiber composites, s_ρ/ρ shows a decreasing trend with higher density ρ . Since the lignocellulosic wood cell walls are essentially homogeneous [31], the density variability is directly related to the heterogeneity of wood's porous microstructure. The porosity is reduced with higher densification, which leads to lower s_ρ/ρ (Fig. 2a). The ratio of ill-posed u ($e \neq 0$) was

reduced to $<0.1\%$ for $r > 0.7$ by carefully selecting the subset size Δ . The exceptions were the neutron radiographs of softwood growth rings (Fig. 4). In this case, unique subset correspondence was only satisfied along one image direction, which led to a minimum of 16 % error values, even with the highest correlation coefficients $r = 0.98$. This scenario is detailed in 4.1.2.

Moisture and Swelling Gradients in Softwood Growth Rings at Hygroscopic Equilibrium

Optical surface deformation measurements

Based on Fig. 2, the anisotropic swelling mechanisms within the growth ring are briefly reviewed [24, 25]. Swelling strains are caused by water sorption in the cell wall and become more pronounced with higher relative humidity RH and adsorbed moisture content ω . The radial strains ϵ_{XX} are thus determined by the cell wall fraction, which scales linearly with the oscillatory growth ring density profile. The intra-ring density profile increases monotonically between EW and LW regions, with a sharp discontinuity at LW-EW transitions (Fig. 5a). In tangential direction, the stiffer LW cells force the EW cells to swell to the same extent, leading to uniform strains ϵ_{YY} . The small shear strains ϵ_{XY} are due to the free swelling of the sample edges.

The strain distributions calculated from optic images with ANRC and commercial DIC were in excellent agreement (Fig. 2c). A quantitative pixel wise comparison revealed rms errors of 0.5 % for ϵ_{XX} and ϵ_{YY} and 0.4 % for ϵ_{XY} . These uncertainties are essentially random and are significantly reduced for the average growth ring profiles (Fig. 2d), with 0.03 % for ϵ_{TB} , 0.11 % for ϵ_{RR} and 0.01 % for ϵ_{RT} . The higher errors for ϵ_{RR} are associated to streaking artifacts (arrows in ϵ_{XX} , Fig. 2c), due to the sharp strain transitions across LW-EW boundaries. The uncertainties were traced back to the u computation (0.05 pixels) and the zero-order search implemented in ANRC. In comparison, the commercial DIC tool uses an iterative scheme incorporating affine subset deformation [27]. This leads to superior accuracy for rotational displacements, but has the drawback of loss of convergence with low correlation statistics, which are typical of texture correlation (TC) [28]. In fact, on the contrary to ANRC, the commercial DIC tool was unable to retrieve u data from neutron radiographs (Fig. 4a, 4.1.2). Since hygromechanical strains are essentially of swelling nature, the zero-order implementation achieves a good trade-off between accuracy and robustness.

Simultaneous neutron imaging of moisture content and moisture-induced deformation

A qualitative comparison of the neutron radiography (Fig. 4a) subsets (I^{ref} , I^{est}) and correlation functions (I^{corr}) with their

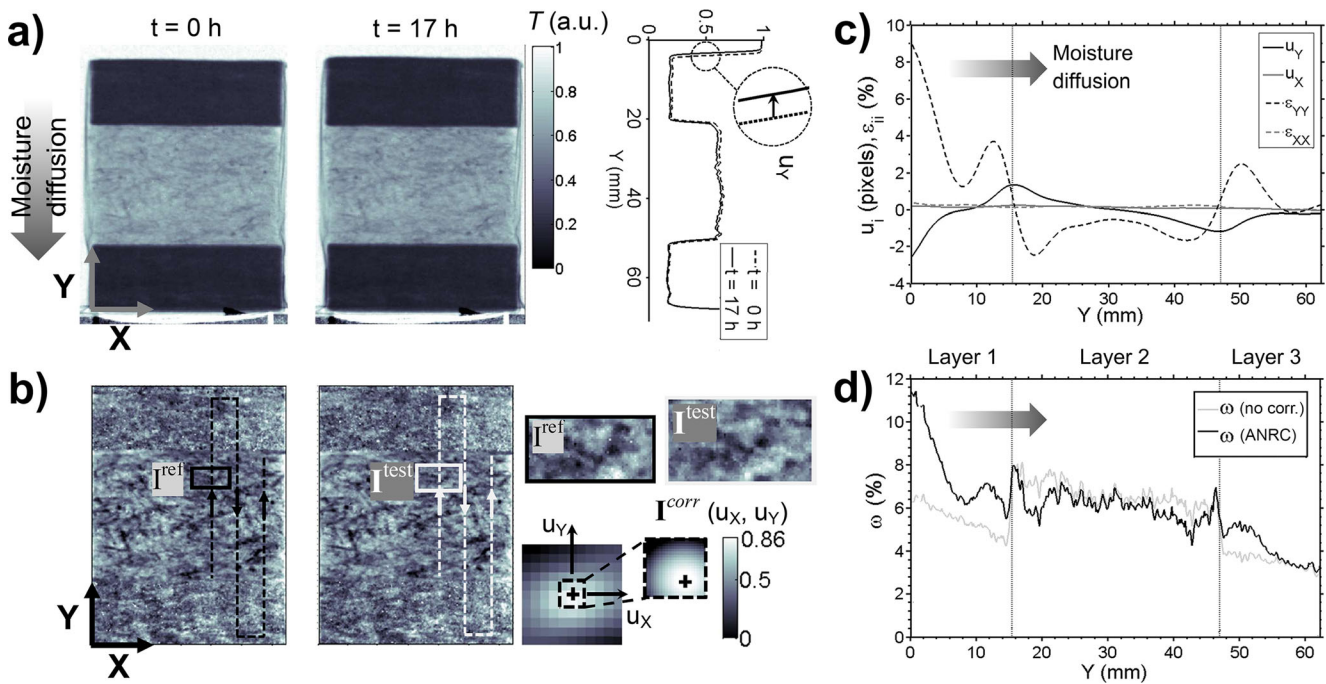


Fig. 7 Applicability of ANRC to investigate hygroscopic transport in highly hygroscopic composites. a) Neutron radiographs of Isoroof-Pavaflex-Isoroof® wood-fiber composite at the beginning ($t=0$ h) and end ($t=17$ h) of unidirectional diffusion experiment. b) Preprocessed

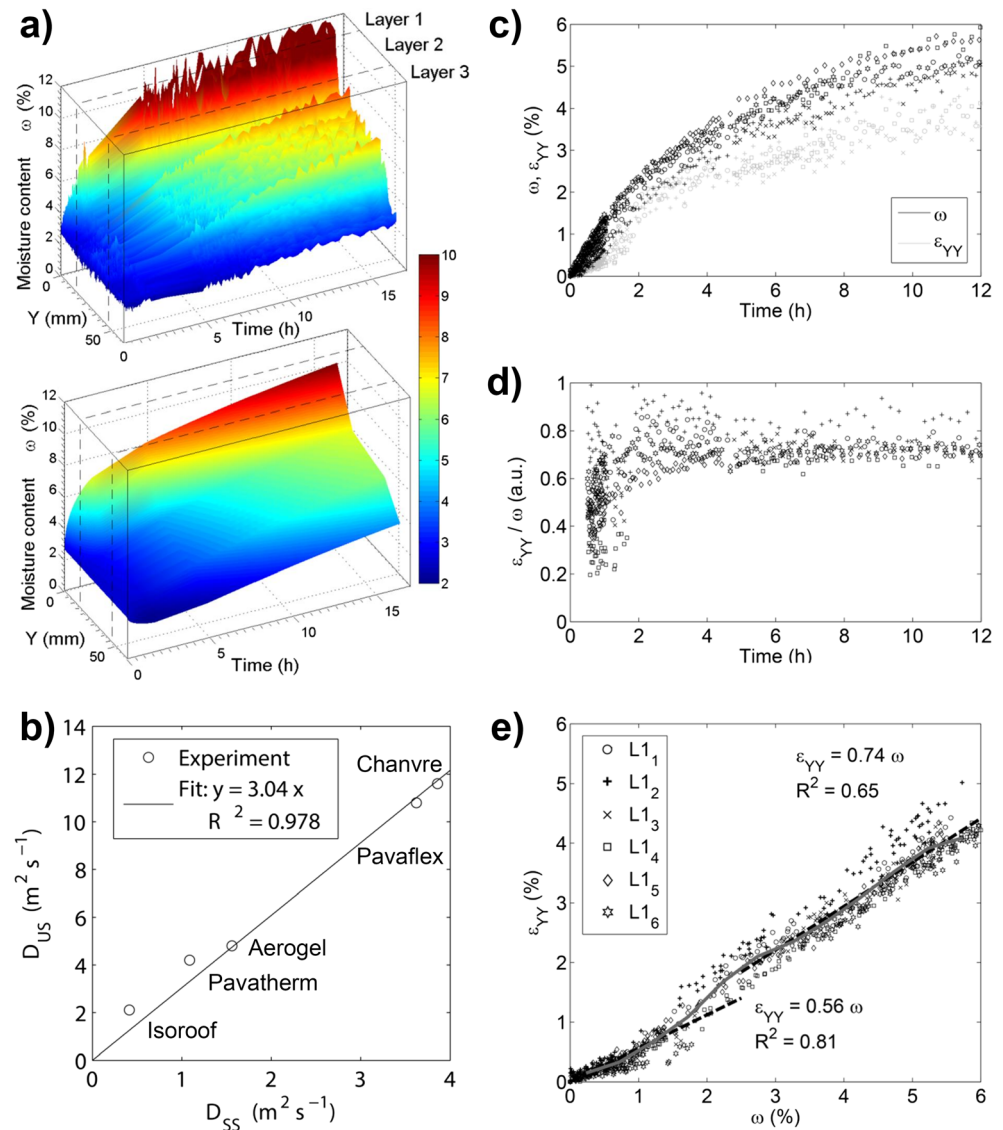
radiographs highlight natural texture. c) Deformation u_y , u_x and strain fields ε_{yy} , ε_{xx} estimated across the thickness Y . d) The deformation correction (ANRC) reveals a negative moisture content ω gradient between moist and dry sample surfaces, in agreement with Fick's Law

optical counterparts of Fig. 2b shows fundamental differences. While the random speckle pattern of the optic images leads to unique correlation peaks, the layered growth ring structure shows quasi-symmetric neutron transmission patterns along the tangential direction Y , which are translated into I^{corr} . Therefore, unique subset correspondence is only poorly satisfied along Y . The ANRC algorithm dealt satisfactorily with this unfavorable deformation tracking scenario. The transmission profiles T in the deformed image were well-aligned with the reference image after correction (Fig. 4b). The ANRC uniqueness and continuity error control correctly sorted out ill-posed deformation values, while preserving the adaptive deformation tracking \hat{u} . The robust reset control ensured that the search region W increased after the maximum error count e_c was exceeded, while rejecting deformation outliers leading to continuity loss (isolated values in u_y profile). The independent error management for u_x and u_y allowed that well-posed u_x were resolved except for 0.5 % of the tracked surface (Table 1). The natural curvature of the growth rings provided enough information to determine u_y for most of the radiograph. The 16 % unresolved u_y pixels (white areas in Fig. 4c) occur at positions where the LW-EW layers are almost parallel to X . A remarkable benchmark of ANRC performance is that the error statistics remained stable with the same algorithm settings for the 60 radiographs analyzed, the adaptive tracking was never lost.

The average strains calculated for each sample and sorption state for neutron (ANRC) and optic (DIC) images agreed closely, with 0.13 % rms error for ε_{RR} and 0.44 % for ε_{TT} (Fig. 6b). Random uncertainties between the deformation fields estimated with both methods (Fig. 4b) were reduced for the average growth ring profiles. The flat ε_{TT} profiles calculated with DIC were closely reproduced with ANRC (Fig. 5b). However, the intra-ring ε_{RR} profiles showed significantly smoother trends for ANRC than for DIC (Fig. 5c). This a consequence of the large subset size Δ required for ANRC ($2.9 \times 2.9 \text{ mm}^2$) in comparison to DIC ($0.7 \times 0.7 \text{ mm}^2$), which matched the mean growth wing width (2.8 mm). For ANRC, the resolution of ε_{RR} was limited by the thin LW layers, which were the dominating texture feature in the radiograph correlation. This led to stepped vertical patterns in u_x , which were not present in the DIC fields (Fig. 4c). Due the resolution loss, the peak value of ε_{RR} in the ANRC profiles was displaced towards the center of the growth ring (Fig. 5b). The same effect is observed by comparing the DIC strains of Fig. 5b with the higher resolution profiles (subset $0.2 \times 0.2 \text{ mm}^2$) of Fig. 2d.

The average ω values calculated with ANRC agreed well with gravimetric measurements (Fig. 6a). Since the calculation of the neutron ω values is based on Equation 1, Fig. 6a experimentally confirms the validity of the neutron mass-attenuation coefficient in water $(\Sigma/\rho)_H = 0.35 \text{ m}^{-2} \text{ kg}^{-1}$ [43] to quantitatively measure bound moisture in wood. The 0.9 % rms uncertainties in ω were equivalent to the reported values with combined neutron/optic DIC measurements, and are

Fig. 8 Simultaneous imaging of hygroscopic moisture transport and swelling in wood-fiber composites. a) Experimental time-space moisture content ω distribution (top) and simulation fit (bottom) for test sample of Fig. 7. b) Regression of unsteady state diffusion coefficients (neutrons) with steady state values (dry/wet cup). c) and d) show the time evolution of ω with respect to thickness swelling ε_{YY} in the moist Isoroof layers for six test samples (L1₁ to L1₆), e) plots together the $(\omega, \varepsilon_{YY})$ pairs, revealing two differentiated hygroscopic swelling regimes



mainly due to residual background neutron scattering induced by the climatic box [15]. Neglecting the swelling strains (No corr.) led to unacceptable ω errors of 5 % for $\varepsilon_{RR} + \varepsilon_{TT}$ up to 8 %, in close agreement with Equation 3. The moisture content ω follows a flat trend within the growth ring, since it scales with the bound water concentration in the cell walls, which in equilibrium conditions is evenly distributed [15, 22]. Combined neutron imaging and optic surface deformation (NI/DIC) confirmed within $\varphi = 0 \dots 0.7$ a constant ω with a rms error of 0.26 % (Fig. 5d, [15]). However, due to the sharp density transition at LW-EW interfaces (Fig. 5a), the region $\varphi = 0 \dots 0.3$ showed strong edge misalignment artifacts and could not be resolved (Fig. 5d). Based only on the neutron radiographs, ANRC successfully removed these artifacts (Fig. 5e), capturing better the volumetric edge information than DIC optic surface measurements. Fig 5e shows a slight peaking around $\varphi = 0.5$, due to the lower resolution of the

estimated ε_{RR} profiles (Fig. 5c) with respect to the neutron radiographs T , T_o (~ 0.7 mm, 3.1.2). This peaking can be removed by pre-smoothing T , T_o to the ANRC subset size (2.9×2.9 mm²) before applying Equation 1 (data not shown). If the NI/DIC experimental setup is available, a better intraring resolution is achieved by aligning the neutron radiographs with ANRC and by inserting in Equation 1 the higher resolution strain fields (0.7×0.7 mm²) calculated with DIC (Fig. 5f). A constant ω with an rms error of 0.18 % is then assessed for the full growth ring $\varphi = 0 \dots 1$.

The discussion is completed by comparing NI and ANRC with other imaging technologies applied in wood science. NMR with isotope selectivity allows moisture measurements without dry state referencing, yet the point-wise testing scheme becomes time-prohibitive for full-field imaging [22]. TC algorithms have been applied to X-ray synchrotron tomograms with micrometer resolution to study hygroscopic cell

wall swelling [32]. At this scale, the high contrast between cell wall and lumen voids allows correlation without need of adaptive search. Non-adaptive TC was indirectly applied to X-ray radiographs of sub-millimeter resolution to monitor wood shrinkage during drying [33]. Dry state images were aligned to specific moisture states with a global pre-registering method, then TC was used to quantify strain out of the transformed dry-state images. In comparison, the proposed ANRC algorithm is able to locally resolve inhomogeneous strain fields, while performing satisfactorily at a resolution scale for which subcellular features are homogenized.

Transient moisture diffusion and moisture-induced swelling in wood-fiber composites

Figure 7a shows neutron radiographs of an Isoroof-Pavaflex-Isoroof composite at the beginning and end of the 17 h diffusion experiment. A profile in thickness direction (Y) clearly reveals the moisture-induced deformation, and shows a strong contrast between the dense outer layers and the lighter middle layer (Table 1). The image preprocessing step (Fig. 7b) improves the lateral resolution of the strain fields by filtering out sample edges and interfaces between composite layers, which would otherwise dominate the correlation process. This highlights the local natural texture, which shows reproducible random patterns in dry I^{ref} and moist I^{est} states that lead to unique correlation peaks in I^{corr} . The peaks are here less sharp than in optical measurements with artificial speckling (Fig. 2b), due to the coarser texture in neutron images, which also requires larger subset sizes ($4.5 \times 9 \text{ mm}^2$). The deformation fields showed complex patterns (Fig. 7c), which were found reproducible for smaller ($3 \times 6 \text{ mm}^2$) and larger ($6 \times 12 \text{ mm}^2$) subset sizes. The up to 11 % thickness swelling strains ε_{YY} were about 20 times larger than in-plane strains ε_{XX} , due to the inner stresses introduced by hot panel pressing, which induce a springback effect [17]. The dense outer layers exerted a strong compressive force upon the lighter middle layer, for which negative strain values were measured. The compressive strains were largest close to the moist layer interface.

Uncorrected for deformation (Fig. 7d), the calculated ω profiles across the composite thickness apparently contradicted Fick's second law, which predicts negative gradients in bound water concentration between moist and dry interfaces [34]. The large thickness swelling strains strongly influenced the calculation, accounting for up to 50 % of ω . After correction, monotonically decreasing ω profiles were obtained, which allowed the optimization of D_{US} with Equation 6. The simulated and experimental time-space moisture distributions were in good agreement, with rms ω errors of 0.6 % (Fig. 8a). The small oscillations at layer interfaces are associated to moisture barrier effects and to volumetric edge artifacts. The optimized unsteady state diffusion coefficients

D_{US} showed a strong correlation ($R^2=0.978$) with the steady state coefficients D_{SS} obtained with the dry/wet cup method (Fig. 8b). The approximately three times scale factor between D_{US} and D_{SS} is consistent with previous observations in solid wood [3], and is associated to the different diffusion regimes and simplifications in the modelling. For instance, the sorption coupling between water vapor and bound water transport, which is a function of the detailed material microstructure and is in general not known, needs to be included in Equation 6 to avoid sample thickness-dependent D_{US} [23].

Figure 8c shows the time evolution of the strain fields ε_{YY} and moisture content ω , averaged over the first Isoroof layer for each of the six tested samples. Both ε_{YY} and ω showed monotonically increasing trends, which flattened at equilibrium moisture content ($t>12 \text{ h}$). The ratio ε_{YY}/ω (Fig. 8d) increased for $t<4 \text{ h}$ and then approached a constant differential swelling q_Y . A time delay of the swelling with respect to the originating moisture content was hypothesized and tested by fitting exponential laws $\varepsilon_{YY}/\omega=q_Y[1-\exp(-t/\tau_\varepsilon)]/[1-\exp(-t/\tau_\omega)]$ to the time-dependent trends of both ε_{YY} and ω . The average $\tau_\omega=5.1 \text{ h}$ and $\tau_\varepsilon=5.8 \text{ h}$ suggest a viscoelastic hygromechanical behavior, with a delay of 0.7 h between moisture and moisture-induced deformation. However, the hypothesis $\tau_\varepsilon<\tau_\omega$ could only be rejected with a t-test above a 20 % confidence level, which throws doubts on such a delay mechanism. Moreover, the flattening of ε_{YY}/ω occurs rather abruptly. Next, a possible moisture-dependent q_Y was tested by plotting all available (ε_{YY}, ω) pairs in a single plot (Fig. 8e), and by extracting a continuous trend with clustering [35]. A master trend between moisture and strain fields was revealed, with differentiated swelling regimes for $\omega<2 \%$ ($\varepsilon_{YY}=0.56 \omega$) and $\omega>3 \%$ ($\varepsilon_{YY}=0.74 \omega$). This behavior can be interpreted by considering that in dry state, the lignocellulosic cell wall shows a low porosity where water molecules find readily available sorption sites (chemisorption). As further sorption takes place (physisorption), the water molecules contribute their full volumes to the cell wall, which is accompanied by higher swelling [7, 36]. The transition region $\omega=2\dots3 \%$ was consistent with observations at hygroscopic equilibrium [37, 38].

Conclusions and Outlook

Neutron imaging together with ANRC processing is able to simultaneously image moisture and moisture-induced deformation fields with high spatial and temporal resolution, with opens new horizons for the hygromechanical characterization of highly swelling materials, as found in wood constructions, but as well in food and agricultural industry, engineering and soil science [6]. One additional advantage of ANRC is that it can be easily implemented as software postprocessing of

neutron images, therefore requiring no modification of available neutron installations.

Applied to the investigation of hygroscopic gradients in softwood growth rings, ANRC provided an excellent agreement with gravimetric moisture content (0.9 % rms error) and optic surface strain measurements (0.5 % error), with similar uncertainties to the ones reported with combined neutron and optic methods. Moreover, ANRC achieved better edge alignment than optic surface deformation measurements [15], allowing to assess a flat moisture trend (0.18 % rms error) even at latewood-earlywood discontinuities. The strain fields estimated with ANRC showed lower resolution than optical measurements, due to the large subset sizes required to capture natural texture. In resolution-critical scenarios, ANRC can be used for radiograph alignment and optic methods can be applied for strain estimation. The ANRC algorithm is readily extensible to three-dimensional stacks as provided by neutron computed tomography. In the hygroscopic range analyzed, the moisture fields were smoother than the texture of the solid phase and represented <10 % of the neutron transmission scale, therefore they did not need to be explicitly accounted for in the correlation procedure. Above saturation, liquid water may lead to stronger contrast differences [19], which can be removed by iteratively subtracting the moisture fields from the radiographs.

Applied to the study of moisture transport in highly hygromorphic wood-fiber composites, the ANRC correction enabled the otherwise not possible optimization of moisture diffusion coefficients, which showed a strong correlation ($R^2=0.978$) with steady state values. Moreover, ANRC provided in-deep understanding of the time development of swelling strains with respect to the originating moisture fields. The results do not clearly support a delay mechanism between strain and moisture fields. However, higher differential swelling coefficients could be assessed in physisorption than in chemisorption regimes. Experimental studies of the rheology of moisture-induced deformation fields have been so far rare, due to the practical challenges in simultaneously mapping time-dependent moisture and strain fields. The ANRC method can contribute to the understanding of mechano-sorptive effects [39]. Another application field is envisaged in the development and characterization of hygromorph composites, which respond to environmental humidity by reproducibly changing their shape [40].

References

- Kardjilov N, Manke I, Hilger A, Strobl M, Banhart J (2011) Neutron imaging in materials science. *Mater Today* 14(6):248–256
- Lehmann E, Vontobel P, Kardjilov N (2004) Hydrogen distribution measurements by neutrons. *App Radiat Isot* 61:503–509
- Mannes D, Sonderegger W, Hering S, Lehmann E, Niemz P (2009) Non-destructive determination and quantification of diffusion processes in wood by means of neutron imaging. *Holzforschung* 63: 589–596
- Perfect E, Cheng CL, Kang M, Bilheux HZ, Lamanna JM, Gragg MJ, et al. Neutron imaging of hydrogen-rich fluids in geomaterials and engineered porous media: a review. *Earth Sci Rev*. 2013.
- Strobl M, Manke I, Kardjilov N, Hilger A, Dawson M, Banhart J (2009) Advanced in neutron radiography and tomography. *J Phys D Appl Phys* 42:243001
- Katekawa ME, Silva MA (2006) A review of drying models including shrinkage effects. *Drying Technol* 24(1):5–20
- Skaar C (1988) *Wood-water relations*. Springer, Berlin
- Bledzki AK, Gassan J (1999) Composites reinforced with cellulose based fibers. *Prog Polym Sci* 24:221–274
- Sonderegger W, Niemz P (2006) Investigation of swelling and thermal expansion of fibreboard, particleboard and plywood. *Eur J Wood Wood Prod* 64:11–20
- Muszynski L (2006) Empirical data for modeling: methodological aspects in experimentation involving hygromechanical characteristics of wood. *Drying Technol* 24(9):1115–1120
- Hussey DS, Sepernjak D, Weber AZ, Mukundan R, Fairweather J, Brosha EL et al (2012) Accurate measurement of the through-plane water content of proton-exchange membranes using neutron radiography. *J Appl Phys* 112:104906
- Derome D, Rafsanjani A, Hering S, Dressler M, Patera A, Lanverman C et al (2013) The role of water in the behavior of wood. *J Build Phys* 36(4):398–421
- Datta AK (2007) Porous media approaches to studying simultaneous heat and mass transfer in food processes II: Property data and representative results. *J Food Eng* 80:96–110
- Mihoubi D, Bellagi A (2012) Modeling of heat and moisture transfers with stress-strain formation during convective air drying of deformable media. *Heat Mass Transfer* 48:1697–1705
- Lanverman C, Sanabria SJ, Mannes D, Niemz P (2014) Combination of neutron imaging (NI) and digital image correlation (DIC) to determine intra-ring moisture variation in Norway spruce. *Holzforschung* 68(1):113–122
- Rosner S, Riegler M, Vontobel P, Mannes D, Lehmann E, Karlsson B et al (2012) Within-ring movement of free water in dehydrating Norway spruce sapwood visualized by neutron radiography. *Holzforschung* 66:751–756
- Sonderegger W, Hering S, Mannes D, P V, Lehmann E, Niemz P. Quantitative determination of bound water diffusion in multilayer boards by means of neutron imaging. *Eur J Wood Wood Prod*. 2010;68:341–350
- Mannes D, Sanabria SJ, Funk M, Wimmer R, Kranitz K, Niemz P. Water vapour diffusion through historically relevant gluten-based wood adhesives with sorption measurements and neutron radiography. *Wood Sci Technol*. 2014;(In print).
- Sedighi-Gilani M, Vontobel P, Lehmann E, Carmeliet J, Derome D. Liquid uptake in Scots pine sapwood and hardwood visualized and quantified by neutron radiography. *Mater Struct*. 2013
- Aregawi W, Defraeye T, Saneinejad S, Vontobel P, Lehmann E, Carmeliet J et al (2013) Dehydration of apple tissue: Intercomparison of neutron tomography with numerical modelling. *Int J Heat Mass Transfer* 67:173–182
- Fu RS, Pasaogullari U, Shiomi T, Tabuchi Y, Hussey DS, Jacobson DL (2012) High-resolution neutron radiography of through-plane liquid water distribution in polymer electrolyte membrane and gas diffusion layer. *J Electrochem Soc* 159(9): F545–F553
- Dvinskikh SV, Henriksson M, Berglund LA, Furó I. A multinuclear magnetic resonance imaging (MRI) study of wood with adsorbed water: estimating bound water concentration and local wood density. *Holzforschung*. 2011;65(103–107).

23. Eitelberger J, Hofstetter K, Dvinskikh SV. A multi-scale approach for simulation of transient moisture transport processes in wood below the fiber saturation point. *Compos Sci Technol*. 2011;71(1727.1738).
24. Lanverman C, Falk W, Niemz P (2014) Full-field moisture induced deformation in Norway spruce: intra-ring variation of transverse swelling. *Eur J Wood Wood Prod* 72:43–52
25. Rafsanjani A, Lanverman C, Niemz P, Carmeliet J, Derome D (2013) Multiscale analysis of free swelling of Norway spruce. *Compos Part A-Appl S* 54:70–78
26. Brombacher V, Michel F, Volkmer T, Niemz P (2012) Investigation of thermal conductivity and moisture behaviour of fibreboard and material combinations. *Bauphysik* 34(4):157–169
27. Sutton MA, Orteu J, Schreier HW (2009) *Image Correlation for Shape, Motion and Deformation Measurements*. Springer, New York, NY, USA
28. Bay BK (2008) *Methods and applications of digital volume correlation*. *J Strain Anal Eng* 43:745
29. De Boor C (2001) *A practical guide to splines*. Springer, New York, NY, USA
30. Michel F. Bestimmung bauphysikalisch relevanter Eigenschaften bei Materialkombination von porösen Holzfaserverplatten und anderen Materialien Bachelor Thesis. Bern University of Applied Sciences - AWCE, 2012
31. Gibson LJ, Ashby MF (1997) *Cellular solids: structure and properties*. Cambridge University Press, Cambridge
32. Forsberg F. X-ray microtomography and digital volume correlation for internal deformation and strain analysis PhD Thesis. Lulea University of Technology, 2008.
33. Watanabe K, Lazarescu C, Shida S, Avramidis S (2012) A novel method of measuring moisture content distribution in timber during drying using CT scanning and image processing techniques. *Drying Technol* 30:256–262
34. Crank J (1975) *The mathematics of diffusion*. Oxford University Press, New York, NY, USA
35. Sanabria SJ, Hilbers U, Neuenschwander J, Niemz P, Sennhauser U, Thömen H et al (2013) Modeling and prediction of density distribution and microstructure in particleboards from acoustic properties by correlation of non-contact high-resolution pulsed air-coupled ultrasound and X-ray images. *Ultrasonics* 53:157–170
36. Derome D, Rafsanjani A, Patera A, Guyer R, Carmeliet J (2012) Hygromorphic behaviour of cellular material: hysteretic swelling and shrinkage of wood probed by phase contrast X-ray tomography. *Phylos Mag A* 92:3680–3698
37. Keylwerth R (1964) Investigations on the course of swelling and the dependence of wood density on moisture. *Eur J Wood Wood Prod* 22: 255–258
38. Popper R, Niemz P, Eberle G (2008) Discussion of the interaction between wood and water based on selected foreign wood species as examples, and the concept of hypothetical hydration water. *Bauphysik* 30(5):333–339
39. Svensson S, Toratti T (2002) Mechanical response of wood perpendicular to grain when subjected to changes of humidity. *Wood Sci Technol* 36:145–156
40. Burgert I, Fratzl P (2009) Actuation systems in plants as prototypes for bioinspired devices. *Phylos Mag A* 367:1541–1557
41. Lehmann EH, Vontobel P, Wiesel L (2001) Properties of the radiography facility NEUTRA at SINQ and its potential for use as a European Reference Facility. *Nondestr Testing Eval* 16:191–202
42. Mannes D, Josic L, Lehmann E, Niemz P (2009) Neutron attenuation coefficients for non-invasive quantification of wood properties. *Holzforschung* 63(4):472–478
43. Hassanein R K. Correction methods for the quantitative evaluation of thermal neutron tomography. PhD Thesis. ETH Zurich, 2006.